

This manuscript is a preprint and has been submitted for publication in *The Journal of Climate*. Please note that this article has not yet undergone peer – review or been formally accepted for publication. Subsequent versions of this manuscript may have slightly different content.

Please feel free to contact any of the authors; we welcome feedback.

1 **Recent water mass changes reveal mechanisms of ocean warming**

2 Jan D. Zika*

3 *School of Mathematics and Statistics, University of New South Wales, Sydney, Australia*

4 Jonathan M. Gregory

5 *National Centre for Atmospheric Science, University of Reading, Reading, UK*

6 Elaine L. McDonagh

7 *NORCE, Norwegian Research Centre, Bjerknes Centre for Climate Research, Bergen, Norway*

8 *and*

9 *National Oceanography Centre, Southampton, UK*

10 Alice Marzocchi and Louis Clement

11 *National Oceanography Centre, Southampton, UK*

12 *Corresponding author: Jan D. Zika, j.zika@unsw.edu.au

ABSTRACT

13 Over 90% of the build up of additional heat in the earth system over recent decades is contained
14 in the ocean. Since 2006 new observational programs have revealed heterogeneous patterns of
15 ocean heat content change. It is unclear how much of this heterogeneity is due to heat being added
16 to and mixed within the ocean leading to material changes in water mass properties or due to
17 changes in circulation which redistribute existing water masses. Here we present a novel diagnosis
18 of the ‘material’ and ‘redistributed’ contributions to regional heat content change between 2006
19 and 2017 based on water mass theory. We show that material warming has large spatial coherence.
20 The material change tends to be smaller than the redistributed change at any geographical location,
21 however it sums globally to the net warming of the ocean, while the redistributed component sums,
22 by design, to zero. Material warming is robust over the time period of this analysis, whereas the
23 redistributed signal only emerges from the variability in a few regions. In the North Atlantic, water
24 mass changes indicate substantial material warming while redistribution cools the subpolar region
25 due to a slowdown in the Meridional Overturning Circulation. Warming in the Southern Ocean is
26 explained by material warming and by anomalous southward heat transport of 118 ± 50 PW due to
27 redistribution. Our results suggest near term projections of ocean heat content change and therefore
28 sea level change will hinge on understanding and predicting changes in ocean redistribution.

29 **1. Introduction**

30 Over the past 50 years, as atmospheric greenhouse gas concentrations have increased, the ocean
31 has absorbed more than ten times as much heat as all other components of the climate system
32 combined (Rhein et al. 2013). This warming showed substantial spatial variability between 1993
33 and 2005, being up to ten times greater in some regions than the global average (Zhang and
34 Church 2012). It is unclear whether this variability is due to geographical variation in the interior
35 propagation of surface warming versus redistribution of existing heat within the ocean.

36 Ocean warming is an important issue because ocean thermal expansion is the largest projected
37 contribution to global mean sea level rise in the 21st century (Church et al. 2013). Numerical
38 climate models disagree on the pattern and amplitude of ocean heat content (OHC) change and
39 hence sea level rise under anthropogenic greenhouse warming (Gregory et al. 2016). Understanding
40 how heat has been taken up and redistributed by the ocean is essential for predicting future changes.

41 Mesoscale eddies and planetary wave processes drive variability in ocean temperature at 10-
42 100km spatial scales and typically dominate differences between ship based observations spaced
43 years apart. Most striking of these is the El Niño Southern Oscillation which lifts the thermocline
44 in the western Pacific and lowers it in the east leading to an exchange of heat between shallow and
45 deep layers. This oscillation dominates observed global mean temperature variability (Roemmich
46 and Gilson 2011).

47 Numerical ocean models forced with historical atmospheric conditions have proved to be useful
48 tools in quantifying the role of atmospheric forcing in setting regional variability in OHC (Drijfhout
49 et al. 2014) and sea level (Penduff et al. 2011). However such models can be ineffective in simulating
50 underlying climate change due to model drift and inaccuracies in model forcing, particularly global
51 mean heat fluxes (Griffies et al. 2009). On the other hand coupled ocean atmosphere climate

52 models are routinely used to capture the effect of climate forcing. But such models only accurately
53 simulate past unforced variability in regional OHC when, by chance, their internal variability is in
54 phase with the observed system.

55 An advancement in terms of numerical ocean climate modeling has been the separation of OHC
56 change into an ‘added’ and a ‘redistributed’ component in climate model simulations, where the
57 former is due to change in the surface heat flux, and the latter due to rearrangement of existing
58 OHC because of altered ocean heat transports (Banks and Gregory 2006). This decomposition
59 is analogous to the ‘anthropogenic’ and ‘natural’ decomposition, that has revolutionized our
60 understanding of oceanic carbon records (Khatiwala et al. 2013). Here we will present a novel
61 method to diagnose the ‘material’ component of OHC change which we will show is closely related
62 the ‘added’ component introduced by Banks and Gregory (2006).

63 Recent work has aimed to reconstruct the drivers of OHC change based on observationally
64 derived air-sea boundary conditions. Zanna et al. (2019) for example used surface temperature
65 anomalies combined with a tracer based approach to reconstruct the role of anomalous surface heat
66 fluxes in centennial heat content change. Roberts et al. (2017) estimated the contribution of air-sea
67 heat flux changes in setting mixed layer and depth integrated OHC budget over recent decades
68 and inferred the role of ocean circulation as a residual. Here we aim to circumvent reliance on
69 such boundary conditions and infer the mechanisms of ocean heat content change directly based
70 on water mass changes.

71 Water mass based methods have been used to decompose local temperature and salinity changes
72 into a dynamic ‘heave’ components and apparently material effects at constant density based on a
73 one dimensional view of the water column (Bindoff and McDougall 1994). However broader scale
74 horizontal motions influence ocean temperature on longer timescales and indeed vertical heaving
75 does not directly affect regional depth integrated OHC.

76 In the present work we present a new method based on water mass theory with which we estimate
77 recent drivers of three dimensional OHC change. In Section 2 we will review water mass theory
78 and establish the relationship between changes in water masses as defined by their temperature and
79 salinity and material changes in sea water temperature. We will describe in Section 3 how this
80 theory is translated into a practical method to estimate material changes in water masses and map
81 these into geographical space. We present results of an application of this method to recent data
82 over the Argo period in Section 4. We discuss the results and compare them with existing work in
83 Section 5 and give conclusions in Section 6.

84 **2. Theory**

85 Water mass analysis has long been used in physical oceanography to trace the origin of waters
86 (Montgomery 1958). In the latter half of the 20th century a quantitative framework emerged to
87 describe the relationship between water masses, air sea fluxes and mixing (Walín 1982). (See
88 the review by Groeskamp et al. (2019).) Recent work has seen this framework advanced in
89 two ways specifically relevant to our work here: to multiple tracer dimensions to understand the
90 thermodynamics of ocean circulation (Nycander et al. 2007; Zika et al. 2012; Döös et al. 2012;
91 Groeskamp et al. 2014; Hieronymus et al. 2014) and to unsteady problems to understand the ocean's
92 role in transient climate change (Palmer and Haines 2009; Evans et al. 2014; Zika et al. 2015a,b;
93 Evans et al. 2017, 2018).

94 An example of the utility of the water mass transformation framework in understanding transient
95 change is provided by Zika et al. (2015a). The distribution of water in salinity coordinates is
96 influenced by the water cycle and turbulent mixing, the latter only being able to collapse the range
97 of salinities the ocean covers. This means that changes in the width of the salinity distribution
98 indicate an enhancement of the water cycle and/or a reduction in that rate at which salt is mixed. In

99 this project we extend this concept to consider how changes in the temperature-salinity distribution
 100 relate to material changes in water masses.

101 Material changes in conservative temperature (here after T) following the motion of an incom-
 102 pressible fluid are related to Eulerian changes and advection by

$$\frac{DT}{Dt} = \frac{\partial T}{\partial t} + \mathbf{u} \cdot \nabla T \quad (1)$$

103 where \mathbf{u} is the 3D velocity vector and $\frac{DT}{Dt}$ is the material derivative which is related to sources
 104 and sinks of heat and irreversible mixing.

105 Even if a perfect record of perfect record of $\frac{\partial T}{\partial t}$ were available at a fixed location, (1) does not
 106 give information regarding the relative roles of advection ($\mathbf{u} \cdot \nabla T$) and material processes ($\frac{DT}{Dt}$). We
 107 therefore consider the water mass perspective as an alternative to the Eulerian perspective. The
 108 following theory draws directly from Hieronymus et al. (2014).

109 We characterize water masses by their T and absolute salinity (here after S). The volume of
 110 water per unit T and S at $T = T^*$ and $S = S^*$ is

$$v(T^*, S^*) = \frac{\partial^2}{\partial T \partial S} \int_{T < T^*, S < S^*} dV. \quad (2)$$

111 Considering all the water in the climate system and retaining the incompressibility assumption,
 112 the only way v can change is via ‘transformation’. That is, by making water parcels warmer, colder,
 113 saltier or fresher. This realization permits the following continuity equation

$$\frac{\partial v}{\partial t} + \frac{\partial}{\partial T} (v\dot{T}) + \frac{\partial}{\partial S} (v\dot{S}) = 0. \quad (3)$$

114 Here \dot{T} is the average material derivative of T within a water mass. That is

$$\dot{T}(T^*, S^*) = \frac{1}{v} \frac{\partial^2}{\partial T \partial S} \int_{T < T^*, S < S^*} \frac{DT}{Dt} dV \quad (4)$$

115 and likewise \dot{S} is the average material derivative of S .

116 In (3) the terms $v\dot{T}$ and $v\dot{S}$ are the transformation rates in the temperature and salinity directions
117 respectively. Equation (3) states that the amount of water between two closely spaced isotherms
118 (T and $T + \partial T$) and isohalines (S and $S + \partial S$) will go up, if more water is made warmer at T than at
119 $T + \partial T$ and/or more water is made saltier at S than at $S + \partial S$ (i.e. more water comes in than goes
120 out).

121 Here we will use changes in v to infer \dot{T} . This will allow us to estimate the material processes
122 influencing ocean temperature change.

123 Note that although $\frac{DT}{Dt}$ is controlled purely by heat sources and sinks and mixing and not ocean
124 circulation. Therefore advection has no role in water-mass ($T-S$) space, presuming it does no
125 mixing, but this does not imply that it has no role in geographical space. Consider for example
126 material warming which is detected within a deep water mass disconnected from the air-sea
127 interface. Heat must have been mixed into that water mass but the heat may have been ‘added’
128 to the sea surface, advected to the deep water mass and then mixed into that water mass. In the
129 Appendix we will indeed show that our water mass based material temperature change corresponds
130 closely with simulated ‘added temperature’ in an ocean model where explicit anomalous heat fluxes
131 are prescribed and the corresponding temperature anomaly is tracked as a tracer throughout the
132 ocean.

133 3. Method

134 Observational estimates of T and S come from the Enact Ensemble (V4.0, here after EN4, Good
135 et al. 2013) for each month between 2006 and 2017 inclusive. We split these data into two periods
136 of time: an ‘early’ period between 2006 and 2011 inclusive and a ‘late’ between 2012 and 2017
137 inclusive. We then define a discrete set of water masses for each time period by splitting the ocean

138 into nine geographical regions and within each region by splitting the ocean up according to T - S
139 bins.

140 Our nine geographical regions are defined: the Southern Ocean south of 35°S , the subtropical
141 Pacific and Atlantic Oceans between 35°S and 10°S , the Indian Ocean north of 35°S , the tropical
142 Pacific and Atlantic Oceans between 10°S and 10°N , the North Pacific north of 10°N , the Atlantic
143 Ocean between 10°N and 40°N and the Atlantic and Arctic Ocean north of 40°N . To avoid
144 discontinuities in our resulting analysis we transition linearly from one region to another over a 10°
145 band (Figure 2).

146 We define T and S bin boundaries ($[T_{min}, T_{max}]$ and $[S_{min}, S_{max}]$ respectively) using a quadtree
147 method. The quadtree method starts with a single (obviously oversized) bin with T boundaries
148 $[-6.4^{\circ}\text{C}, 96^{\circ}\text{C}]$ and S boundaries $[-5.2\text{g/kg}, 46\text{g/kg}]$ in which the entirety of the ocean's sea
149 water resides. The single bin is then split into 4 equally sized bins with the same aspect ratio as
150 the original bin. The same process of splitting into four is repeated for any bin whose volume
151 change is greater than a threshold of $62 \times 10^{12}\text{m}^3$ (equivalent to the volume of a 5° longitude by
152 5° latitude region at the equator with a depth of 200m) or until the bin size is 0.4°C by 0.2g/kg .
153 In the supplementary text we show that changing the size of these bins by a factor of two does not
154 substantially change our results.

155 The quadtree method is applied within each region and for the change between the late and early
156 periods. This results in bin edges defining 1447 water masses. These bins are then used to define
157 both the 'early water masses' and the 'late water masses'.

158 The i th early water mass is described by its geographical region (from one to nine), its volume
159 ($V1_i$), its volume weighted mean temperature ($T1_i$) and its volume weighted mean salinity ($S1_i$,
160 Fig. 2). Likewise, the j th late water mass is described by its region, volume ($V2_j$), temperature
161 ($T2_j$) and salinity ($S2_j$).

162 To change the water mass distribution from that of the early period to that of the late period
 163 requires that water be ‘transformed’ in T – S space. When water transforms it changes its T and S
 164 either in the same geographical region or as it moves to a region nearby. Transformation between
 165 early and late water masses is described by a matrix g . The i th column and j th row (g_{ij}) corresponds
 166 to the average transformation of water from early water mass i to late water mass j in units of m^3
 167 s^{-1} over some time period Δt . Note that even if the i th water mass for the early period has the
 168 same temperature and salinity bounds as the i th water mass of the late period, the distribution of
 169 properties within the bin can change, so the average temperature and salinity of the water within
 170 the bin can change. That is, in general $T1_i \neq T2_i$ and $S2_i \neq S1_i$, so g_{ij} is always a ‘transformation’,
 171 even with $i = j$.

172 Since the total volume of water is conserved from the early to late periods the following volume
 173 budget is applied

$$V1_i = \Delta t \sum_{j=1}^N g_{ij} \quad \text{and} \quad V2_j = \Delta t \sum_{i=1}^N g_{ij}. \quad (5)$$

174 Our goal is to estimate the matrix g . Out of the infinite number of choices which could satisfy
 175 (5), we find a ‘minimum transformation’, using an Earth Mover Distance (EMD) algorithm (Pele
 176 and Werman 2008, 2009). The EMD solves the hypothetical problem of moving earth from a set
 177 of mounds, each with varying amounts of earth, into a set of holes with varying amounts of empty
 178 space to be filled. The optimization problem is to find the smallest total mass weighted distance
 179 that needs to be travelled in order to empty the mounds and fill the holes. In our case the ‘mounds’
 180 are the early water masses and the ‘holes’ are the late water masses.

181 For the EMD algorithm, we require a ‘distance’ metric (D), which is a matrix whose i th column
 182 and j th row (d_{ij}) is the cost of moving from the i th early water mass to the j th late water mass.

183 The EMD algorithm then estimates g such that (5) is satisfied and the following total transport
 184 weighted ‘distance’ travelled is minimized

$$\sum_{j=1}^N \sum_{i=1}^N g_{ij} d_{ij}. \quad (6)$$

185 We use the following distance metric

$$d_{ij} = (T1_i - T2_j)^2 + [a(S1_i - S2_j)]^2 + \delta_{ij} \quad (7)$$

186 where temperature and salinity differences are squared so that long trajectories in T – S space are
 187 penalized more than short ones and a is an arbitrary constant which scales the salinity change
 188 relative to the temperature change. The intent of δ_{ij} is to permit water masses to move across our
 189 arbitrary geographical boundaries without penalty but at the same time to stop direct exchange
 190 between geographically disconnected regions, for example between the Southern Ocean and Arctic
 191 or the tropical Atlantic and tropical Pacific. To achieve this we set $\delta_{ij} = 0$ where the i th and j th
 192 water masses are in the same or adjacent geographical regions and $\delta_{ij} = \infty$ otherwise. Regions
 193 which share a meridional boundary are considered adjacent. The Arctic and North Pacific are not
 194 considered adjacent while the Indian Ocean and equatorial Pacific regions are considered adjacent.

195 We choose the constant a to be the ratio of a typical haline contraction coefficient to a typical
 196 thermal expansion coefficient ($a = \beta_0/\alpha_0 = 4.28$). This does not mean that transformations along
 197 density surfaces are necessarily preferred. The squares in (7) mean that density compensated
 198 changes in T and S are penalized as much as changes of the same magnitude where one of the signs
 199 is reversed. We have tested the sensitivity of the method to varying a by a factor of two and found
 200 only negligible changes in inferred warming (see the Appendix).

201 By moving water from a temperature $T1_i$ to $T2_j$, the transformation g_{ij} implies warming or
 202 cooling of a portion of the i th early water mass, transforming it into a portion of the j th late

203 water mass. To gain a picture of the net material change within a water mass we add up all the
 204 warming/cooling necessary to transform the i th early water mass into all of its destination water
 205 masses to derive an average material warming rate (\dot{T}_i) within each early water mass

$$\dot{T}_i = \frac{1}{V1_i} \sum_{j=1}^N (T2_j - T1_i) g_{ij}. \quad (8)$$

206 which is shown in Fig. S1.

207 We now aim to use \dot{T} to define a 3D material temperature change variable $\Delta T_{Material}$. To do this
 208 we make the assumption that the warming of a particular water mass occurred evenly (in a volume
 209 and time weighted sense) over the regions and times during which that water mass existed in the
 210 early period. E.g. if a particular location was occupied by the n th water mass for the entire period
 211 2006 to 2011, then the inferred rate of change of material temperature at that location would have
 212 been \dot{T}_n . Likewise, if the n th water mass occupied that location between 2006 and 2008 and the
 213 m th water mass existed there between 2009 and 2011, then the rate of change of material heat
 214 content will be $(\dot{T}_n + \dot{T}_m)/2$. More precisely, at every location \mathbf{x} we define $T_{Material}$ as

$$\Delta T_{Material}(\mathbf{x}) = \int_{t_1}^{t_2} \sum_{i=1}^N \Pi(T(\mathbf{x}), [T_i^{min}, T_i^{max}]) \Pi(S(\mathbf{x}), [S_i^{min}, S_i^{max}]) \dot{T}_i dt.$$

215 Above, Π is a boxcar function such that $\Pi(T, [T_1, T_2])=1$ when $T_1 \leq T < T_2$ and 0 otherwise and
 216 t_1 the start of 2006 and t_2 is the end of 2011.

217 We could equally have attributed warming to each late water mass based on how much heat was
 218 required to transform the early water masses into the late water mass. We find the above approach
 219 more intuitive. The difference between maps of material heat content change made using the two
 220 approaches are well within the uncertainties stated (not shown).

221 We will contrast the inferred material warming at \mathbf{x} against the total warming $\Delta T(\mathbf{x}) = T(\mathbf{x}, t_2) -$
222 $T(\mathbf{x}, t_1)$ with the residual of the two being a redistribution component such that

$$\Delta T_{Material} = \Delta T - \Delta T_{Redistribution} \quad (9)$$

223 In the Appendix we compare results of our method applied to synthetic data from a climate model
224 simulation to an added heat variable explicitly simulated by the model. We find good agreement
225 between added heat and our inferred $\Delta T_{Material}$ and between simulated redistributed heat and
226 inferred $\Delta T_{Redistribution}$ when ocean temperature and salinity are fed in as ‘data’ to the method.
227 The Appendix also explores sensitivity of our results to parameter choices. The uncertainties we
228 place on OHC change are ± 2 standard deviations of a bootstrap ensemble, also described in the
229 Appendix.

230 To produce maps of the total, material and redistributed contributions to the heat content we
231 multiply the density and heat capacity of sea water by the respective temperature change and
232 vertically integrate these through the entire water column. Our method also produces a material
233 salinity change. We leave discussion of those data to future work.

234 4. Results

235 Patterns of total OHC change between early and late periods are heterogeneous (Fig. 3A). There
236 are basin scale patches of decreasing heat content in the western equatorial and tropical Pacific, in
237 the Pacific sector of the Southern Ocean, in the subtropical south Indian Ocean, and the subtropical
238 North Atlantic. Warming is seen most strongly in the tropical eastern Pacific, south Atlantic Ocean
239 and subtropical North Atlantic. These changes are highly sensitive to the specific observation years
240 chosen and the length of the epochs reflecting the regional timescale of variability associated with
241 the redistributed component. Uncertainty is far larger than the signal in the majority of regions

242 (stippling in Fig. 3A) and coincident with previously-identified regions of large sea level anomaly
243 variability (Penduff et al. 2011). However, there are a few regions (e.g. the Southern Ocean and
244 North Atlantic) where the regional redistributed signal is robust and emerges from the uncertainty
245 (Fig. 3B).

246 Material heat content change shows a smaller amplitude but more coherent signal than redis-
247 tributed heat (Figs. 3B and 3C). Material warming is seen across almost the entirety of the globe,
248 with maxima in the Southern Hemisphere and Atlantic subtropical convergence zones (Maximenko
249 et al. 2009), consistent with model simulations of passive ocean heat uptake due to anthropogenic
250 greenhouse warming (Gregory et al. 2016). Strikingly however, the uncertainty in material heat
251 content change is far smaller than that of total OHC change (stippling in Fig. 3C). This suggests
252 that heat was added to and distributed within the ocean persistently over the Argo period and that
253 this warming is not an artifact of a particularly warm year or years.

254 Zonally integrating the net OHC change reveals a signal of roughly the same magnitude as its
255 uncertainty at all latitudes (Fig. 4A). Zonally integrated redistributed heat likewise has a small
256 signal to uncertainty ratio except in the Southern Ocean (Fig. 4A). Accumulating the redistributed
257 heat contribution from north to south gives the meridional heat transport due to redistribution.
258 Broadly, heat is redistributed from north to south with a southward cross equatorial transport of 73
259 ± 60 TW between the two epochs (Fig. 4C).

260 Material heat content change is larger than its uncertainty at most latitudes and shows a peak at
261 35°S , 15°N and 35°N . The material heat content change peaks at 35°S and 35°N are collocated
262 with climatological wind stress curl minima, which drive Ekman downwelling.

263 Table 1 shows material, redistributed and total heat content changes by ocean basin. Material
264 heat content change is distributed among the Indian, South Pacific and South Atlantic basins
265 approximately according to their area. However, the North Atlantic stores close to 25% of the

266 global ocean's material heat content change despite representing less than 12% of its area (Table
267 1). An outsized role for the Atlantic and Southern Ocean in storing material heat content change in
268 the climate system has also been foreseen in numerical modeling studies (Lee et al. 2011; Kuhlbrodt
269 and Gregory 2012).

270 We identify robust redistributed warming signals in the sub-tropical North Atlantic and Southern
271 Ocean. Warming in the sub-tropical North Atlantic is compensated by cooling in the sub-polar
272 North Atlantic consistent with a 40 ± 13 TW southward transport of heat across 44°N (Fig. 3C,
273 Fig. 4C). Warming in the Southern Ocean is far larger and explained by 118 ± 50 PW of southward
274 heat transport across 32°S .

275 **5. Discussion**

276 Recent anomalous southward heat transport in the North Atlantic has been well documented
277 and has been attributed to a downturn in the Atlantic Meridional Overturning Circulation (Smeed
278 et al. 2013; Bryden et al. 2020). Observed heat transport anomalies equate to a downturn in MHT
279 equivalent to -23 ± 60 TW for the period 2006-2011 vs 2012-2017 at 26°N in the Atlantic (see the
280 Appendix for details of this calculation which is based on data from Bryden et al. 2020) which is
281 consistent with our estimate of the change in redistribution heat transport of -23 ± 19 TW (Fig. 4,
282 uncertainties are ± 2 standard deviations).

283 The large apparent meridional heat transport we have identified in the Southern Ocean was
284 previously identified by Roberts et al. (2017) based on the residual of observed OHC change and
285 estimates of air sea heat fluxes. Their approach captures additional heat in the system where it
286 is fluxed into the ocean while our approach estimates how that heat is distributed. Nonetheless,
287 the correspondence between our results and theirs is reassuring and perhaps not surprising if the
288 redistribution signal is large as both approaches indicate.

289 The approach of Zanna et al. (2019) is more directly comparable to ours. They reconstruct the
290 passive contribution to ocean warming since 1850 by propagating SST anomalies into the ocean
291 interior using Green's functions. They compare their inferred passive warming between 1955 and
292 2016 to the warming observed in situ and find evidence of a large southward redistribution of heat
293 in the Northern Hemisphere. This may suggest that the southward redistribution of heat inferred by
294 both Roberts et al. (2017) and this study in the Southern Hemisphere is a more recent occurrence.

295 **6. Conclusions**

296 In conclusion we have shown that:

- 297 • Water mass changes between 2006-2011 and 2012-2017 can be interpreted in terms of a
298 material warming across the globe, concentrated most strongly in the Southern Ocean and
299 North Atlantic, consistent with simulations of the addition of heat into the ocean due to green
300 house forcing;
- 301 • The majority of the pattern of ocean heat content change over that period can be explained by
302 a redistribution of existing water masses within the ocean;
- 303 • The inferred redistribution indicates a downturn in northward meridional heat transport into
304 the sub-polar North Atlantic of 40 ± 13 TW and an anomalous southward heat transport into
305 the Southern Ocean of 118 ± 50 TW.

306 The material warming signal we have inferred is generally weaker than redistribution, but the
307 signal is far less sensitive to changes in the years over which the analysis was carried out. This
308 suggests material warming may be giving a robust indication of slow thermodynamic changes in
309 the ocean, potentially as a result of anthropogenic forcing. This would be remarkable since there
310 are only 6 years between the centre of the early and late periods we have considered.

311 We expect the strength of the material warming signal to increase into the future as the ocean
312 warms. However since the redistribution signal is so large, circulation changes and variability must
313 be understood if near term regional sea level change is to be projected accurately.

314 *Acknowledgments.* We would like to acknowledge the UK Met Office’s Hadley Centre for main-
315 taining the EN4 data set used here and Professors O. Pele and M. Werman for developing and
316 making available their Earth Mover Distance code. We thank John Church, Richard Sanders and
317 Lijing Cheng for helpful suggestions regarding this manuscript.

318 JZ was supported by Australian Research Council Grant DP190101173. EM, AM and LC were
319 supported by Natural Environment Research Council grant NE/P019293/1 (TICTOC) and EM was
320 also supported by European Union Horizon 2020 grant 817578 (TRIATLAS). JG was supported
321 by Natural Environment Research Council grants NE/P019099/1 (TICTOC) and NE/R000727/1
322 (UK-FAFMIP).

323 *Data availability statement.* Analyzed temperature and salinity data used in
324 this study was from EN4 (Good et al. 2013) and is publicly available at
325 <https://www.metoffice.gov.uk/hadobs/en4/download-en4-2-1.html>.

326 Code used to convert EN4 in-situ temperature and practical salinity fields to con-
327 servative temperature and absolute salinity were from the Gibbs Sea-Water Oceano-
328 graphic Toolbox available at <http://www.teos-10.org/software.htm#1>. Code which im-
329 plements the methods described in the Methods Section are available at drop-
330 box.com/sh/wl1ry8lbf6m56mv/AABIBWi5blAucyzEQQWXF2oVa?dl=0 and will be made avail-
331 able in a stable online repository before publication. The aforementioned code includes FastEMD
332 (Pele and Werman 2008, 2009) software available at <http://www.cs.huji.ac.il/~ofirpele/FastEMD/>.

334 Accuracy of the warming estimates we have produced rely on the following assumptions:

- 335 1. The mapping from transformations in $T - S$ space for each region to local changes in geo-
336 graphical space is accurate;
- 337 2. The ‘minimum transformation’ inferred using the EMD algorithm, including our choice of
338 distance metric, accurately estimates the net thermodynamic transformation;
- 339 3. The resolution of our T-S grid is sufficiently fine to capture relevant water masses; and
- 340 4. The density of observations and the procedure used to map them onto a regular grid is
341 sufficiently accurate for us to quantify changes in water mass volumes.

342 We investigate the impact of each of these assumptions in the supplementary text. We investigate
343 1 and 2 using synthetic data from a climate model where ‘added heat’ is explicitly simulated
344 (Section 1) and we investigate 3 and 4 using sensitivity tests (Section 2 and Section 3). A bootstrap
345 approach is taken in the latter case to derive uncertainty estimates.

346 **A1. Validation using synthetic data**

347 We use synthetic data from the Hadley Centre Climate Model version HadCM3 (Gordon et al.
348 2000) to validate the method described in the methods section. Specifically, we exploit the con-
349 figuration used for the Flux Anomaly Forced Model Inter-comparison Project (FAFMIP, Gregory
350 et al. 2016). We will consider two specific model experiments used by FAFMIP: *piControl*, which
351 is a reference experiment with no external forcing, and *FAFheat*, where the ocean is warmed by
352 an imposed surface heat flux.

353 In *FAFheat* ‘added temperature’ (T_{added}) and ‘redistributed temperature’ (T_{redist}) tracers are
354 simulated explicitly. T_{added} is simulated as a passive tracer initialized at zero and forced at the
355 ocean boundary by the imposed heat flux anomaly. T_{redist} is simulated, again, as a passive tracer,

356 which is initialized with the true ocean temperature at the start of the perturbation experiment and
357 does not increase with the imposed heat flux anomaly but continues to respond to all other fluxes of
358 heat at the sea surface within the coupled climate model. By construction the T in $FAFheat$ is the
359 sum of the T_{added} and T_{redist} . Unlike the redistributed heat inferred using our method, T_{redist} can be
360 a net non-zero contributor to ocean heat content. This is because in both $piControl$ and $FAFheat$
361 the surface heat flux can vary because of unforced fluctuations which are not constrained to sum
362 to zero, and in $FAFheat$ it is modified also due to changes in sea surface temperature, caused by
363 changes in ocean circulation, arising from buoyancy forcing by the imposed heat perturbation. For
364 more details of this phenomenon and of FAFMIP in general see Gregory et al. (2016).

365 There are two aspects of our method which we aim to validate using these data: the uncertainty
366 introduced by 1) projecting an inferred warming signal from temperature and salinity classes (water
367 masses) to the geographical location of those water masses and 2) using the Earth Mover Distance
368 Algorithm.

369 The FAFMIP protocol does not describe historical climate change but rather an idealized increase
370 in ocean heat content as would be expected from a doubling in atmospheric CO₂. Our observational
371 record is centered on the beginning of 2012 when the global atmospheric CO₂ concentration reached
372 392 parts per million (Conway et al. 1994), which is approximately 40% above pre-industrial levels
373 of approximately 280 parts per million. Although no comparison can be perfect, we consider this
374 reasonable motivation to choose years 35-46 of the FAFMIP experiments to test our method.

375 HadCM3 conserves potential temperature and a salinity variable initialized based on observed
376 practical salinity, so we use these to define temperature and salinity respectively for the purposes
377 of defining water masses in this analysis.

378 *a. Validation of the water mass based projection*

379 Fig. A4 a shows the column integral of the added heat tracer for years 41 to 46 for the HadCM3
380 *FAFheat* experiment (the tracer is represented in Kelvin but is here converted to more familiar
381 W/m² by multiplying by the heat capacity and density and dividing by 43 years). As was done to
382 the EN4 data, we selected water mass bins using a quadtree approach. Fig. A4b shows column
383 integrated added heat change between years 41-46, but in this case where the added heat tracer is
384 first averaged within each water mass within each of the 9 geographical regions, then projected back
385 into the location of those water masses. What this projection amounts to is simply homogenizing the
386 added heat tracer within each water mass in each region. If added heat change varies substantially
387 within a water mass this method will smooth out those variations. In the zonal mean (Fig. A4c)
388 the re-projected added heat has an RMS error of 0.5 TW/°lat.

389 *b. Validation of the Earth Mover Distance based method*

390 We will test our method in the following three scenarios:

- 391 1. Added heat only - heat is added to the ocean and water masses are not redistributed;
- 392 2. Redistribution only – no heat is added and water masses are redistributed;
- 393 3. Added and redistributed heat – Heat is added and water masses are redistributed.

394 Table A1 details the way data from *piControl* and *FAFheat* are used for these scenarios.

395 1) SCENARIO 1

396 In this scenario there is no explicit ‘redistribution’ signal in the model data. The purpose of this
397 validation is to see how much of the change is attributed to material heat content change using our
398 water mass change approach. In the zonal mean (Fig. A4A) the difference between the simulated

399 and inferred added heat (which is precisely the inferred redistributed heat) has an RMS of 1.8
400 TW/°lat.

401 2) SCENARIO 2

402 In this scenario there is no explicit ‘added heat’ signal in the model data. This is simply a climate
403 control run with no variations in forcing (solar, aerosol etc). There is, however, some very small
404 changes in ocean heat uptake due to natural variability in the fluxes of heat at the air-sea interface.
405 The purpose of this validation is to see how much of the change is attributed to our redistributed
406 heat using our water mass change approach. In the zonal mean (Fig. A4B) the difference between
407 the simulated heat content change and the inferred redistributed heat (which is precisely the inferred
408 added heat) has an RMS of 0.4 TW/°lat.

409 3) SCENARIO 3

410 In this scenario there is both an explicit ‘added heat’ signal in the model data and the model
411 redistributes heat in response to both natural variability and the imposed warming. Despite the
412 inclusion of a non-zero global mean net surface heat flux in FAFMIP redistributed heat (as described
413 above), it is instructive to see how well our material and redistributed heat estimates compare to
414 the directly simulated added and redistributed heat variables. In the zonal mean (Fig. A4C)
415 the difference between both the simulated FAFMIP added heat content and the inferred material
416 heat content change and between the simulated FAFMIP redistributed heat and our water mass
417 based redistributed heat, has an RMS of 2.4 TW/°lat. We emphasize that this difference should not
418 necessarily be directly attributed to an inaccuracy in our method considering the differing meanings
419 of redistributed heat between the model simulations and our method. Broadly we consider the
420 stated differences between directly simulated and inferred changes to be acceptable. We made no

421 attempt to tune method parameters to optimize correspondence with the simulated variables, but
422 this could be pursued in future.

423 **A2. Parameter sensitivity**

424 Here we test the sensitivity of the results, in particular the zonally integrated added heat, to
425 parameter choices within the water mass method.

426 The two choices were: i) the choice of relative penalty on temperature versus salinity changes
427 (i.e. parameter ‘a’) and ii) the number of water masses in T-S space used to represent the early and
428 late ocean states. We discuss sensitivity to these choices here.

429 The reference case for a is the ratio of a constant haline contraction coefficient ($\beta_0 = 7.55 \times 10^{-4}$
430 $\text{kg} / (\text{g/kg}) \text{ m}^3$) to a constant thermal expansion coefficient ($\alpha_0 = 1.76 \times 10^{-4} \text{ kg} / \text{K m}^3$; i.e. a_0
431 $= \alpha_0 / \beta_0 = 4.3\text{K} / (\text{g} / \text{kg})$). This choice implies a transformation by 1g/kg in absolute salinity
432 is penalized equivalently to a transformation of 4.3K in temperature. A larger a will cause the
433 method to favor transformation along the S axis and a smaller a will favor transformation along the
434 T axis. We test the method in the following cases: $a = a_0$; $a_0/2$ and $2*a_0$ (Fig. A4A) and find RMS
435 differences of 0.3 TW / °lat between the reference case and the doubling and halving cases.

436 In terms of $T - S$ resolution, our reference case has a minimum $T - S$ bin size of 0.2 g / kg and
437 0.4 K. Using the quadtree method the grid is refined until either this resolution is achieved or the
438 volume within a particular bin falls below $62 \times 10^{12} \text{ m}^3$. We test the sensitivity of this choice by
439 both refining and coarsening the resolution by a factor of two in both the salinity and temperature
440 dimensions and reducing the volume threshold by a factor of four also.

441 Decreasing the resolution induces an RMS change in estimated zonally averaged OHC of 0.5
442 TW/°lat and increasing the resolution induces an RMS change of 0.4 TW/°lat (Fig. A4B).

443 **A3. Robustness of 21st Century trend**

444 To quantify the sensitivity of our trend results to the time period chosen and the specific obser-
445 vations made and mapped in that period, we carry out a bootstrap calculation. Our aim here is
446 not to determine how accurate our trend is, but rather to determine how representative it is of time
447 period as a whole or if specific years strongly influence the result.

448 We chose to subsample the data by including and excluding entire years from the analysis. Six
449 years are used for the early (2006-2011) and late (2012-2017) periods of our analysis of EN4. We
450 therefore considered all possible permutations of the numbers one to six and re-ran our analysis of
451 EN4 subsampling the years corresponding to those six numbers. For example, in the case [1, 3, 3,
452 4, 5, 6] the ‘early period’ data was replaced with the years 2006, 2008 repeated twice, 2009, 2010
453 and 2011 and the ‘late period’ with 2012, 2014 repeated twice, 2015, 2016 and 2017.

454 There are 46656 uniquely ordered permutations of the numbers one to six when repetition is
455 permitted. Since the calculation is insensitive to the order of the six years for either the early or
456 late period, in practice we only need to consider the 462 unique permutations (ignoring order) and
457 weight each by its frequency in the larger set of ordered permutations.

458 Fig. 3 shows the mean while Fig. A4 shows the standard deviation of the bootstrap ensemble.
459 Plus and minus two standard deviations of the spread in estimates of zonally averaged heat content
460 change are shown in Fig. 4. Since these error estimates are generally larger than our other parameter
461 sensitivity tests, we use them as our formal uncertainties throughout the main text.

462 **A4. Comparison with Atlantic meridional heat transport trend at 26°N**

463 We will compare our estimate of the contribution of redistribution to MHT north of 26°N in the
464 Atlantic (Fig. 4C) with data reported by Bryden et al. (2020) (Tab. A4). MHT relates to the rate of
465 change of OHC. That is $MHT = \partial OHC / \partial t$. The difference in OHC between two year (for example

466 2006 and 2012) relates to MHT via

$$\int_{2006}^{2012} MHT dt = OHC(2012) - OHC(2006). \quad (A1)$$

467 We have considered the difference in OHC between two 6 year periods (2006-2011 versus 2012-
468 2017). Hence our OHC change and MHT are related via

$$\begin{aligned} \left(\int_{t_0}^{t_0+\Delta t} OHC(t) dt - \int_{t_0-\Delta t}^{t_0} OHC(t) dt \right) = \\ \int_{t_0}^{t_0+\Delta t} (OHC(t) - OHC(t - \Delta t)) dt = \\ \int_{t_0}^{t_0+\Delta t} \int_{t-\Delta t}^t MHT(t') dt' dt \end{aligned} \quad (A2)$$

469 where t_0 is midnight on the 31st December 2012 and Δt is 6 years. In practice we have averages of
470 MHT covering April-March (see table A4), we approximate (A2) using 6 year running means of
471 MHT then averaging these between 2009-2010 and 2014-2015. Our uncertainties are \pm two times
472 the standard deviation of the 6-year running means.

473 **References**

- 474 Banks, H. T., and J. M. Gregory, 2006: Mechanisms of ocean heat uptake in a coupled climate
475 model and the implications for tracer based predictions of ocean heat uptake. *Geophysical*
476 *Research Letters*, **33** (7).
- 477 Bindoff, N. L., and T. J. McDougall, 1994: Diagnosing climate change and ocean ventilation using
478 hydrographic data. *Journal of Physical Oceanography*, **24**, 1137–1152.
- 479 Bryden, H. L., W. E. Johns, B. A. King, G. McCarthy, E. L. McDonagh, B. I. Moat, and D. A.
480 Smeed, 2020: Reduction in ocean heat transport at 26°n since 2008 cools the eastern subpolar
481 gyre of the north atlantic ocean. *Journal of Climate*, **33** (5), 1677–1689.

- 482 Church, J., and Coauthors, 2013: *Sea Level Change*, book section 13, 1137–1216. Cam-
483 bridge University Press, Cambridge, United Kingdom and New York, NY, USA, doi:
484 10.1017/CBO9781107415324.026, URL www.climatechange2013.org.
- 485 Conway, T. J., P. P. Tans, L. S. Waterman, K. W. Thoning, D. R. Kitzis, K. A. Masarie, and N. Zhang,
486 1994: Evidence for interannual variability of the carbon cycle from the national oceanic and
487 atmospheric administration/climate monitoring and diagnostics laboratory global air sampling
488 network. *Journal of Geophysical Research: Atmospheres*, **99 (D11)**, 22 831–22 855.
- 489 Döös, K., J. Nilsson, J. Nycander, L. Brodeau, and M. Ballarotta, 2012: The World Ocean
490 Thermohaline Circulation. *Journal of Physical Oceanography*, **42**, 1445–1460.
- 491 Drijfhout, S. S., A. T. Blaker, S. A. Josey, A. Nurser, B. Sinha, and M. Balmaseda, 2014: Surface
492 warming hiatus caused by increased heat uptake across multiple ocean basins. *Geophysical*
493 *Research Letters*, **41 (22)**, 7868–7874.
- 494 Evans, D. G., J. Toole, G. Forget, J. D. Zika, A. C. Naveira Garabato, A. G. Nurser, and L. Yu, 2017:
495 Recent wind-driven variability in atlantic water mass distribution and meridional overturning
496 circulation. *Journal of Physical Oceanography*, **47 (3)**, 633–647.
- 497 Evans, D. G., J. D. Zika, A. C. Naveira Garabato, and A. Nurser, 2014: The imprint of southern
498 ocean overturning on seasonal water mass variability in drake passage. *Journal of Geophysical*
499 *Research: Oceans*, **119 (11)**, 7987–8010.
- 500 Evans, D. G., J. D. Zika, A. C. Naveira Garabato, and A. G. Nurser, 2018: The cold transit of
501 southern ocean upwelling. *Geophysical Research Letters*, **45 (24)**, 13–386.

- 502 Good, S. A., M. J. Martin, and N. A. Rayner, 2013: EN4: Quality controlled ocean temperature
503 and salinity profiles and monthly objective analyses with uncertainty estimates. *Journal of*
504 *Geophysical Research: Oceans*, **118** (12), 6704–6716.
- 505 Gordon, C., C. Cooper, C. A. Senior, H. Banks, J. M. Gregory, T. C. Johns, J. F. Mitchell, and R. A.
506 Wood, 2000: The simulation of sst, sea ice extents and ocean heat transports in a version of the
507 hadley centre coupled model without flux adjustments. *Climate dynamics*, **16** (2-3), 147–168.
- 508 Gregory, J. M., and Coauthors, 2016: The flux-anomaly-forced model intercomparison project
509 (FAFMIP) contribution to CMIP6: investigation of sea-level and ocean climate change in
510 response to CO₂ forcing. *Geoscientific Model Development*, **9** (11), 3993.
- 511 Griffies, S. M., and Coauthors, 2009: Coordinated Ocean-ice Reference Experiments (COREs).
512 *Ocean Modelling*, **26**, 1–46.
- 513 Groeskamp, S., S. M. Griffies, D. Iudicone, R. Marsh, A. G. Nurser, and J. D. Zika, 2019: The
514 water mass transformation framework for ocean physics and biogeochemistry. *Annual review of*
515 *marine science*, **11**, 271–305.
- 516 Groeskamp, S., J. D. Zika, T. J. McDougall, B. M. Sloyan, and F. Laliberté, 2014: The represen-
517 tation of ocean circulation and variability in thermodynamic coordinates. *Journal of Physical*
518 *Oceanography*, **44** (7), 1735–1750.
- 519 Hieronymus, M., J. Nilsson, and J. Nycander, 2014: Water mass transformation in salinity–
520 temperature space. *Journal of Physical Oceanography*, **44** (9), 2547–2568.
- 521 Khatiwala, S. P., and Coauthors, 2013: Global ocean storage of anthropogenic carbon. *Biogeo-*
522 *sciences*, **10** (4), 2169–2191.

523 Kuhlbrodt, T., and J. M. Gregory, 2012: Ocean heat uptake and its consequences for the magnitude
524 of sea level rise and climate change. *Geophysical Research Letters*, **39** (18), L18 608.

525 Lee, S.-K., W. Park, E. van Sebille, M. O. Baringer, C. Wang, D. B. Enfield, S. G. Yeager, and
526 B. P. Kirtman, 2011: What caused the significant increase in atlantic ocean heat content since
527 the mid-20th century? *Geophysical Research Letters*, **38** (17).

528 Maximenko, N., P. Niiler, L. Centurioni, M.-H. Rio, O. Melnichenko, D. Chambers, V. Zlotnicki,
529 and B. Galperin, 2009: Mean dynamic topography of the ocean derived from satellite and drifting
530 buoy data using three different techniques. *Journal of Atmospheric and Oceanic Technology*,
531 **26** (9), 1910–1919.

532 Montgomery, R. B., 1958: Water characteristics of atlantic ocean and of world ocean. *Deep Sea*
533 *Research* (1953), **5** (2-4), 134–148.

534 Nycander, J., J. Nilsson, K. Döös, and G. Bromström, 2007: Thermodynamic analysis of Ocean
535 Circulation. *Journal of Physical Oceanography*, **37**, 2038–2052.

536 Palmer, M. D., and K. Haines, 2009: Estimating oceanic heat content change using isotherms.
537 *Journal of Climate*, **22** (19), 4953–4969.

538 Pele, O., and M. Werman, 2008: A linear time histogram metric for improved sift matching.
539 *European conference on computer vision*, Springer, 495–508.

540 Pele, O., and M. Werman, 2009: Fast and robust earth mover’s distances. *2009 IEEE 12th Inter-*
541 *national Conference on Computer Vision*, IEEE, 460–467.

542 Penduff, T., M. E. Juza, B. Barnier, J. D. Zika, W. K. Dewarr, A.-M. Treguier, J.-M. Molines,
543 and N. Audiffren, 2011: Sea Level Expression of Intrinsic and Forced Ocean Variabilities at
544 Interannual Time Scales. *Journal of Climate*, **24**, 5652–5670.

545 Rhein, M., and Coauthors, 2013: Observations: ocean.

546 Roberts, C. D., M. D. Palmer, R. P. Allan, D. G. Desbruyeres, P. Hyder, C. Liu, and D. Smith, 2017:
547 Surface flux and ocean heat transport convergence contributions to seasonal and interannual
548 variations of ocean heat content. *Journal of Geophysical Research: Oceans*, **122** (1), 726–744.

549 Roemmich, D., and J. Gilson, 2011: The global ocean imprint of enso. *Geophysical Research*
550 *Letters*, **38** (13).

551 Smeed, D., and Coauthors, 2013: Observed decline of the atlantic meridional overturning circula-
552 tion 2004 to 2012. *Ocean Science Discussions*, **10** (5), 1619–1645.

553 Walin, G., 1982: On the relation between sea–surface heat flow and thermal circulation in the
554 ocean. *Tellus*, **34**, 187–195.

555 Zanna, L., S. Khatiwala, J. M. Gregory, J. Ison, and P. Heimbach, 2019: Global reconstruction of
556 historical ocean heat storage and transport. *Proceedings of the National Academy of Sciences*,
557 **116** (4), 1126–1131.

558 Zhang, X., and J. A. Church, 2012: Sea level trends, interannual and decadal variability in the
559 pacific ocean. *Geophysical Research Letters*, **39** (21).

560 Zika, J. D., M. H. England, and W. P. Sijp, 2012: The Ocean Circulation in Thermohaline
561 Coordinates. *Journal of Physical Oceanography*, **2**, 708–724, doi:10.1175/JPO-D-11-0139.1.

562 Zika, J. D., F. Laliberté, L. R. Mudryk, W. P. Sijp, and A. Nurser, 2015a: Changes in ocean vertical
563 heat transport with global warming. *Geophysical Research Letters*, **42** (12), 4940–4948.

564 Zika, J. D., N. Skliris, A. G. Nurser, S. A. Josey, L. Mudryk, F. Laliberté, and R. Marsh, 2015b:
565 Maintenance and broadening of the ocean’s salinity distribution by the water cycle. *Journal of*
566 *Climate*, **28** (24), 9550–9560.

567 **LIST OF TABLES**

568 **Table 1.** Heat content change by ocean basin in TW. Estimates are based on differences
569 between the periods 2006-2011 and 2012-2017 inclusive. Uncertainties are \pm
570 two standard deviations. The Southern Ocean is defined as the entire ocean
571 south of 32°S . The South Pacific, South Atlantic and Indian Ocean estimates
572 exclude the ocean south of 32°S . The North Atlantic is split into a region south
573 and a region north of 44°N . The later includes the Arctic Ocean. 29

574 **Table A1.** Summary of data used for three validation scenarios. T_{ref} and S_{ref} are the
575 temperatures and salinities from the *piControl* experiment respectively. T_{added}
576 is the added heat variable and T_{redist} is the redistributed heat variable from
577 the *FAFheat* experiment. S_{heat} is the salinity variable from the *FAFheat*
578 experiment. The numbers in brackets are the experiment years chosen (e.g.
579 $T_{ref}(41-46)$ is temperature from years 41 to 46 of the piControl experiment). 30

580 **Table A2.** Atlantic meridional heat transport (MHT, in PW) at 26°N (Bryden et al. 2020),
581 MHT anomaly relative to 2006-2017 and 6-year running mean MHT. The mean
582 of 6-year running means is relevant to the difference in OHC between 2006-2011
583 and 2012-2017. 31

584 TABLE 1. Heat content change by ocean basin in TW. Estimates are based on differences between the periods
 585 2006-2011 and 2012-2017 inclusive. Uncertainties are \pm two standard deviations. The Southern Ocean is defined
 586 as the entire ocean south of 32°S. The South Pacific, South Atlantic and Indian Ocean estimates exclude the
 587 ocean south of 32°S. The North Atlantic is split into a region south and a region north of 44°N. The later includes
 588 the Arctic Ocean.

	Material	Redistributed	Total
Southern Ocean	90 \pm 18	118 \pm 50	208 \pm 63
South Pacific	53 \pm 16	-26 \pm 22	28 \pm 22
North Pacific	82 \pm 25	-61 \pm 55	21 \pm 54
Indian Ocean	45 \pm 10	-13 \pm 25	32 \pm 30
South Atlantic	34 \pm 11	6 \pm 7	40 \pm 7
North Atlantic (< 44°N)	75 \pm 33	20 \pm 17	95 \pm 46
North Atlantic (> 44°N)	19 \pm 6	-40 \pm 13	-20 \pm 16
Global Ocean	398 \pm 81	0	398 \pm 81

589 Table A1. Summary of data used for three validation scenarios. T_{ref} and S_{ref} are the temperatures and
590 salinities from the *piControl* experiment respectively. T_{added} is the added heat variable and T_{redist} is the
591 redistributed heat variable from the *FAFheat* experiment. S_{heat} is the salinity variable from the *FAFheat*
592 experiment. The numbers in brackets are the experiment years chosen (e.g. $T_{ref}(41-46)$ is temperature from
593 years 41 to 46 of the piControl experiment).

Scenario	Early period	Late period
1	$T = T_{ref}(41-46),$ $S = S_{ref}(41-46)$	$T = T_{ref}(41-46) + T_{added}(41-46)$ $S = S_{ref}(41-46)$
2	$T = T_{ref}(35-40)$ $S = S_{ref}(35-40)$	$T = T_{ref}(41-46)$ $S = S_{ref}(41-46)$
3	$T = T_{added}(35-40) + T_{redist}(35-40)$ $S = S_{ref}(35-40)$	$T = T_{added}(41-46) + T_{redist}(41-46)$ $S = S_{heat}(41-46)$

595 Table A2. Atlantic meridional heat transport (MHT, in PW) at 26°N (Bryden et al. 2020), MHT anomaly
 596 relative to 2006-2017 and 6-year running mean MHT. The mean of 6-year running means is relevant to the
 597 difference in OHC between 2006-2011 and 2012-2017.

Year	MHT	Anomaly	6-year mean
2006-2007	1.37	0.178	-
2007-2008	1.3	0.108	-
2008-2009	1.23	0.038	-
2009-2010	0.91	-0.282	0.018
2010-2011	1.19	-0.002	-0.038
2011-2012	1.26	0.068	-0.043
2012-2013	1.03	-0.162	-0.057
2013-2014	1.27	0.078	-0.011
2014-2015	1.15	-0.042	-0.007
2015-2016	1.18	-0.012	-
2016-2017	1.22	0.028	-
		Mean	-0.023
		Std	0.029

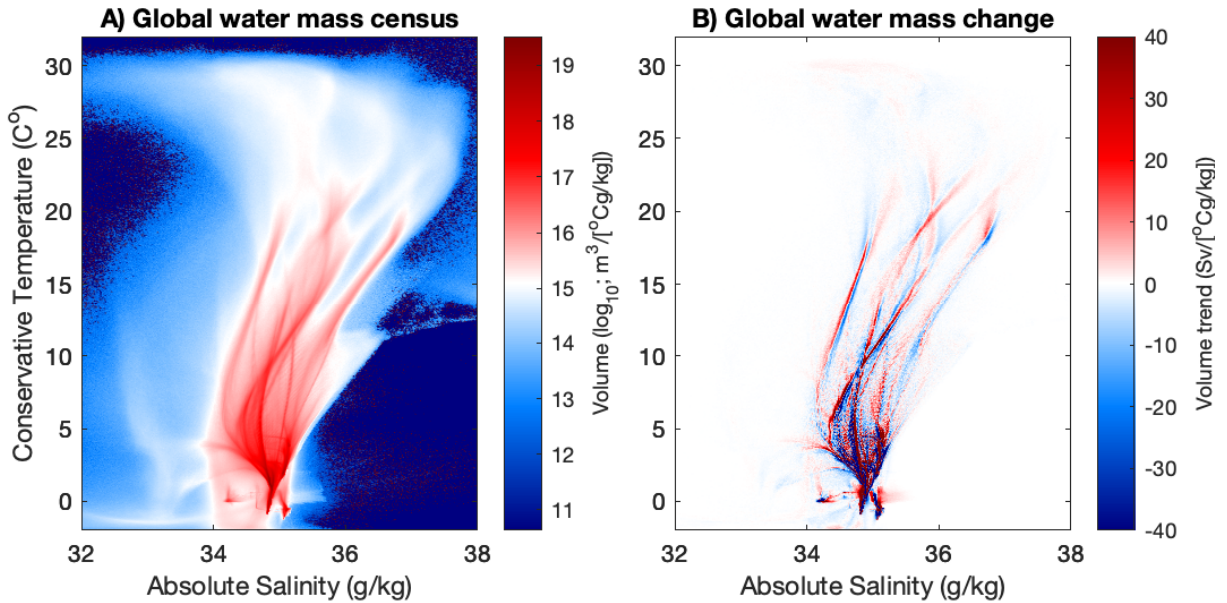
598

LIST OF FIGURES

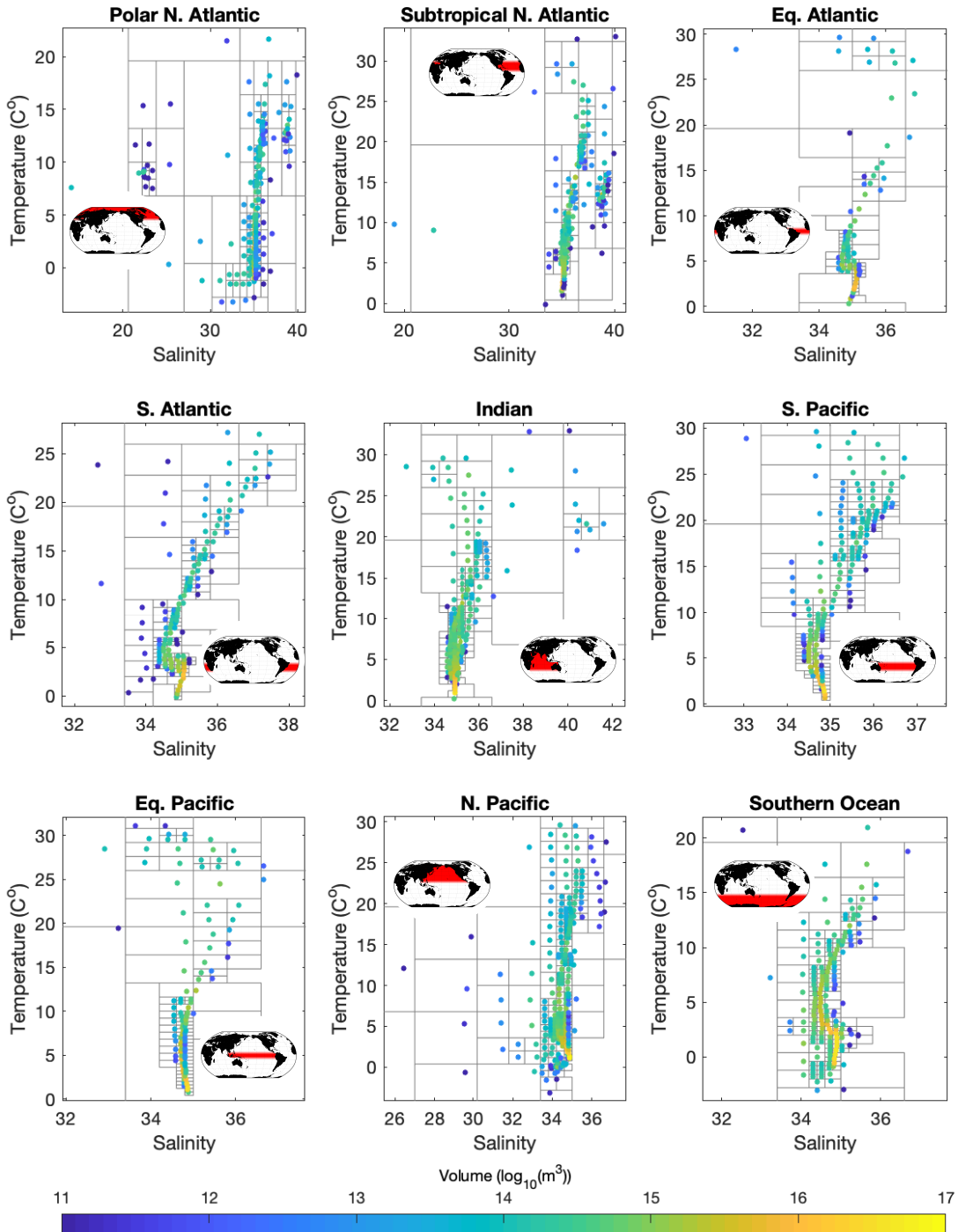
599		
600	Fig. 1.	Portrait of changing ocean water masses. A: Inventory of ocean volume in conservative temperature versus absolute salinity coordinates (mean of 2006 to 2017 inclusive). B: Change in water mass volume between the early half and late half of the period divided by the six years ($Sv = 106m^3/s$). According to water mass theory, changes in air-sea heat and fresh water fluxes and/or changes in rates of diffusion are required for these changes to occur. 34
601		
602		
603		
604		
605	Fig. 2.	Grey lines show conservative temperature, T , and absolute salinity, S , bounds of each water mass (or ‘bin’) generated by the quadtree method for each geographical region. The average T and S of the water found within each bin is shown by the location of each marker and the volume is represented by the color scale ($\log_{10}(m^3)$). Inventories and mean T and S values represent the entire period (2006-2017 inclusive). Inset panels show masks associated with each geographical region. 35
606		
607		
608		
609		
610		
611	Fig. 3.	Heterogeneous pattern of total and redistributed heat content change contrast against robust material heat content change. A: Change in depth integrated ocean heat content between years 2006-2011 and 2012-2017 inclusive. B: Inferred redistributed heat and C: Inferred material heat content change based on changing water masses for the same period. Regions where the magnitude of the signal is less significant (less than two standard deviations of a bootstrap ensemble) are stippled. 36
612		
613		
614		
615		
616		
617	Fig. 4.	Material heat content change is accumulating in the tropics and sub-tropics existing heat is being redistributed southward. A: Total heat content change (grey) redistribution contribution (blue) and material contribution (red). B: Contributions to material heat content change from the Indian (green), Pacific (orange) and Atlantic (yellow) Oceans. C: Meridional heat transport due to redistribution in the Southern Ocean (blue), Atlantic (cyan) and Indian plus Pacific Oceans (magenta). Estimates are bootstrap ensemble means with shading representing \pm two standard deviations. 37
618		
619		
620		
621		
622		
623		
624	Fig. S1.	Each marker shows $\Delta T_{material}$, the average warming required for each early water mass in order to transform them into the set of late water masses. 38
625		
626	Fig. S2.	A: Directly simulated added heat by the FAFheat experiment averaged over years 41-46 of the experiment. B: Inferred added heat when the same FAFheat data is first homogenized in water masses (bins in temperature-salinity coordinates) then remapped into the locations of those water masses over the same period. C: Comparison of the zonal integration of the two quantities shown in A and B. 39
627		
628		
629		
630		
631	Fig. S3.	A: Zonally integrated simulated added heat (solid, red) and inferred material heat content change (dashed, red) based on our water mass method for years 41-46 of the <i>FAFheat</i> experiment comparing the simulation with and without added heat. B: Zonally integrated simulated heat content change (solid, blue) and inferred redistributed heat (dashed, blue) based on our water mass method comparing years 35-40 and 41-46 of the <i>piControl</i> experiment. C: Zonally integrated simulated added heat (solid, red) and redistributed heat (blue, solid) in the <i>FAFheat</i> experiment and inferred material heat content change (dashed, red) and redistributed heat (dashed, blue) based on our water mass method applied the model data. 40
632		
633		
634		
635		
636		
637		
638		
639	Fig. S4.	A: Zonally integrated inferred material heat content change for cases where the parameter a is set at a reference value of $a_0 = \alpha_0 / \beta_0 = 4.3K/(g/kg)$ (black) and then reduced (red) and increased (blue) by a factor of two. B: Zonally integrated inferred material heat content change for cases where the $T - S$ bins are shrunk using a quadtree method until they either contain a volume of sea water less than $62 \times 10^{12}m^3$ or have a bin size of $0.4^\circ C$ by $0.2 g/kg$
640		
641		
642		
643		

644 (black). Cases where the minimum volume is $15.5 \times 10^{12} \text{ m}^3$ and the minimum bin size is
645 0.2°C by 0.1g/kg (blue) and where the minimum volume is $248 \times 10^{12} \text{ m}^3$ and the minimum
646 bin size is 0.8°C by 0.4g/kg (red). 41

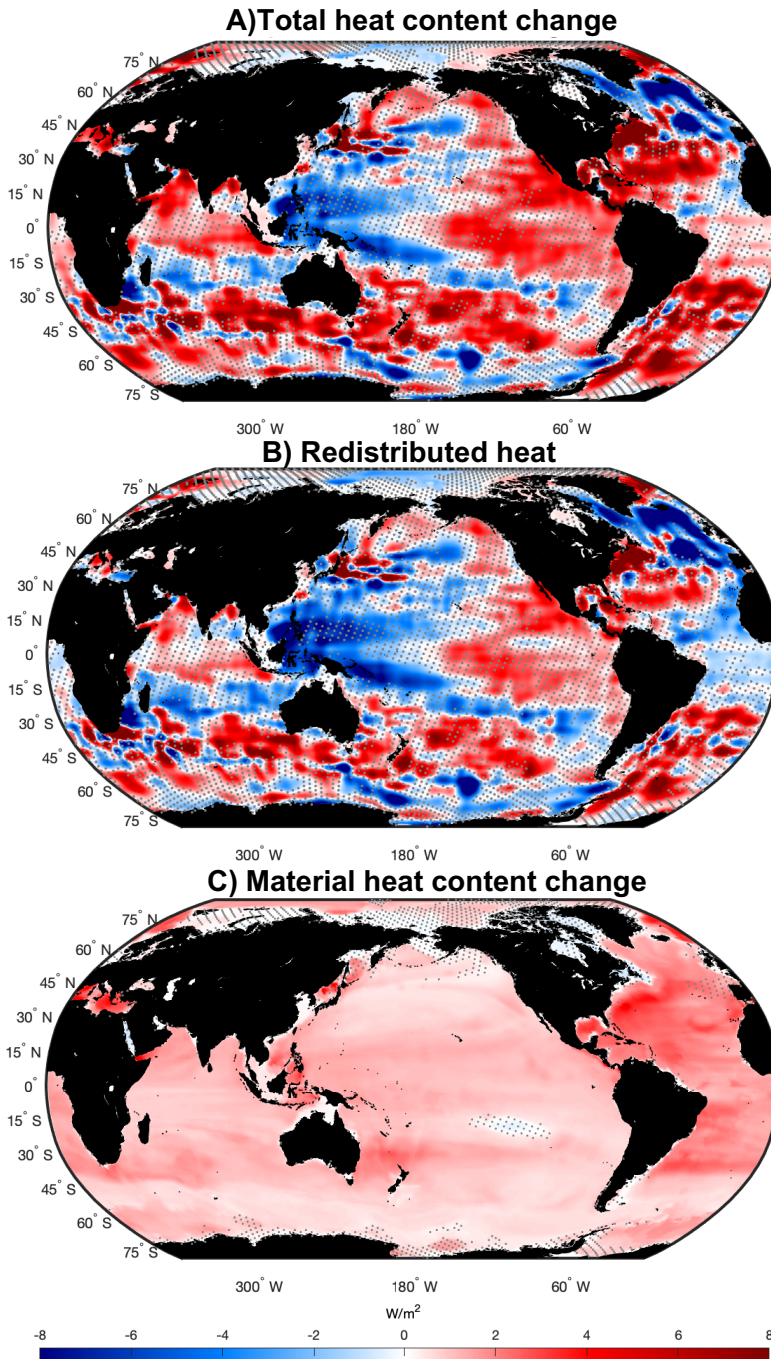
647 **Fig. S5.** A: One standard deviation of the heat content change inferred based on subsampling ‘early’
648 and ‘late’ years of the EN4 data set. One standard deviation of the ensemble of inferred
649 material heat content change (B) and redistributed heat (C) based on our water mass method
650 applied to the same subsampled data as in A. 42



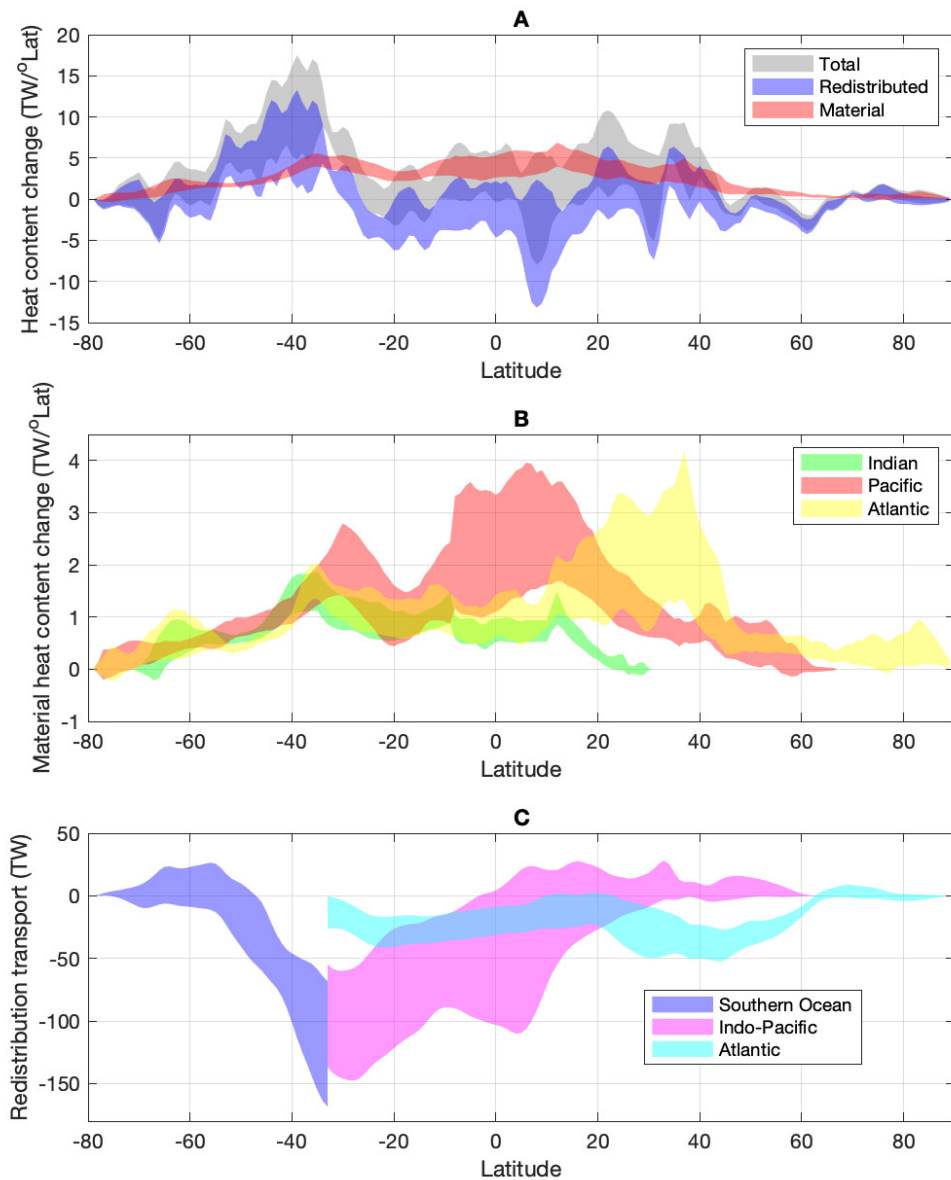
651 FIG. 1. Portrait of changing ocean water masses. A: Inventory of ocean volume in conservative temperature
 652 versus absolute salinity coordinates (mean of 2006 to 2017 inclusive). B: Change in water mass volume between
 653 the early half and late half of the period divided by the six years ($\text{Sv} = 106\text{m}^3/\text{s}$). According to water mass theory,
 654 changes in air-sea heat and fresh water fluxes and/or changes in rates of diffusion are required for these changes
 655 to occur.



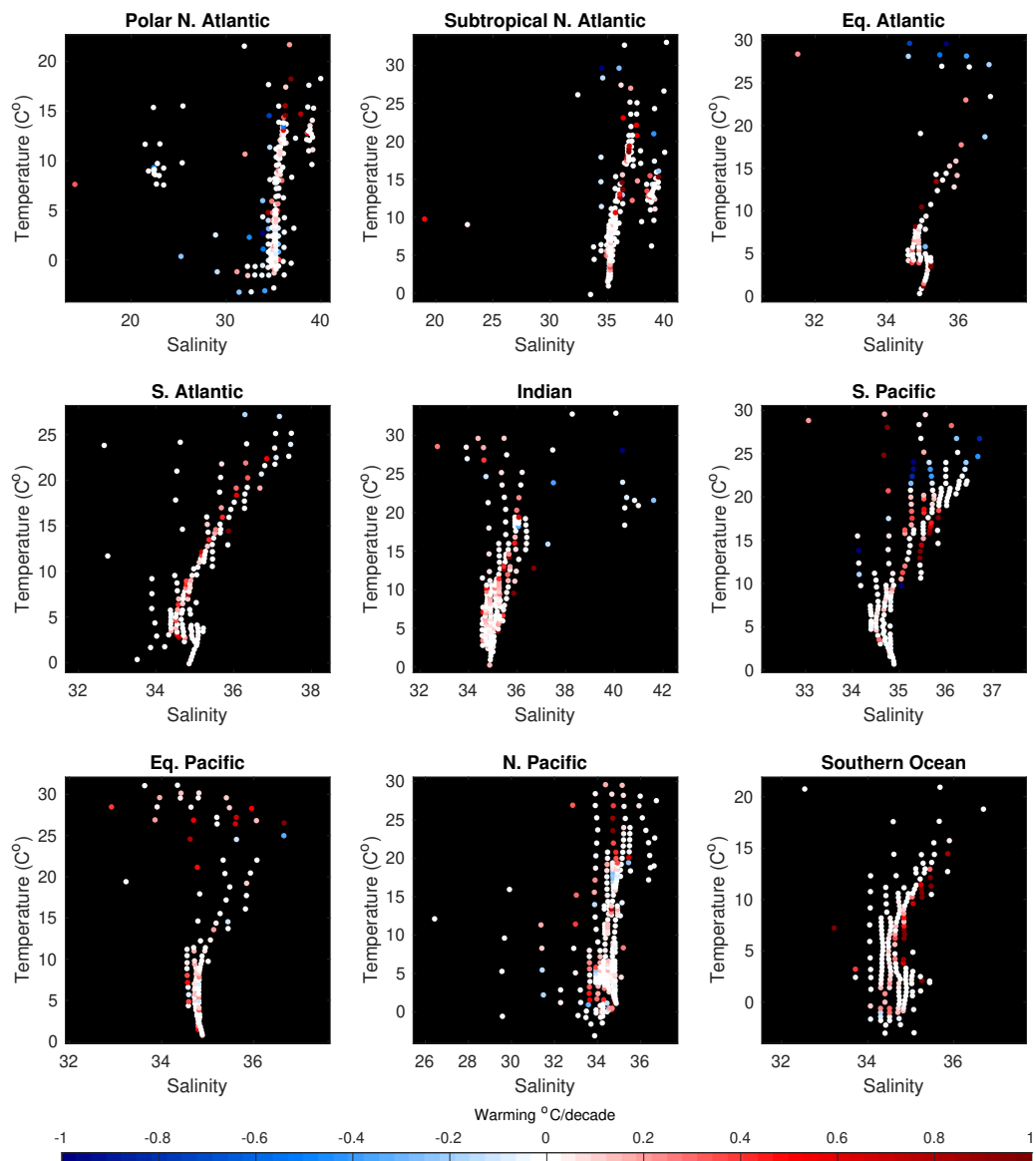
656 FIG. 2. Grey lines show conservative temperature, T , and absolute salinity, S , bounds of each water mass
 657 (or ‘bin’) generated by the quadtree method for each geographical region. The average T and S of the water
 658 found within each bin is shown by the location of each marker and the volume is represented by the color scale
 659 ($\log_{10}(\text{m}^3)$). Inventories and mean T and S values represent the entire period (2006–2017 inclusive). Inset panels
 660 show masks associated with each geographical region.



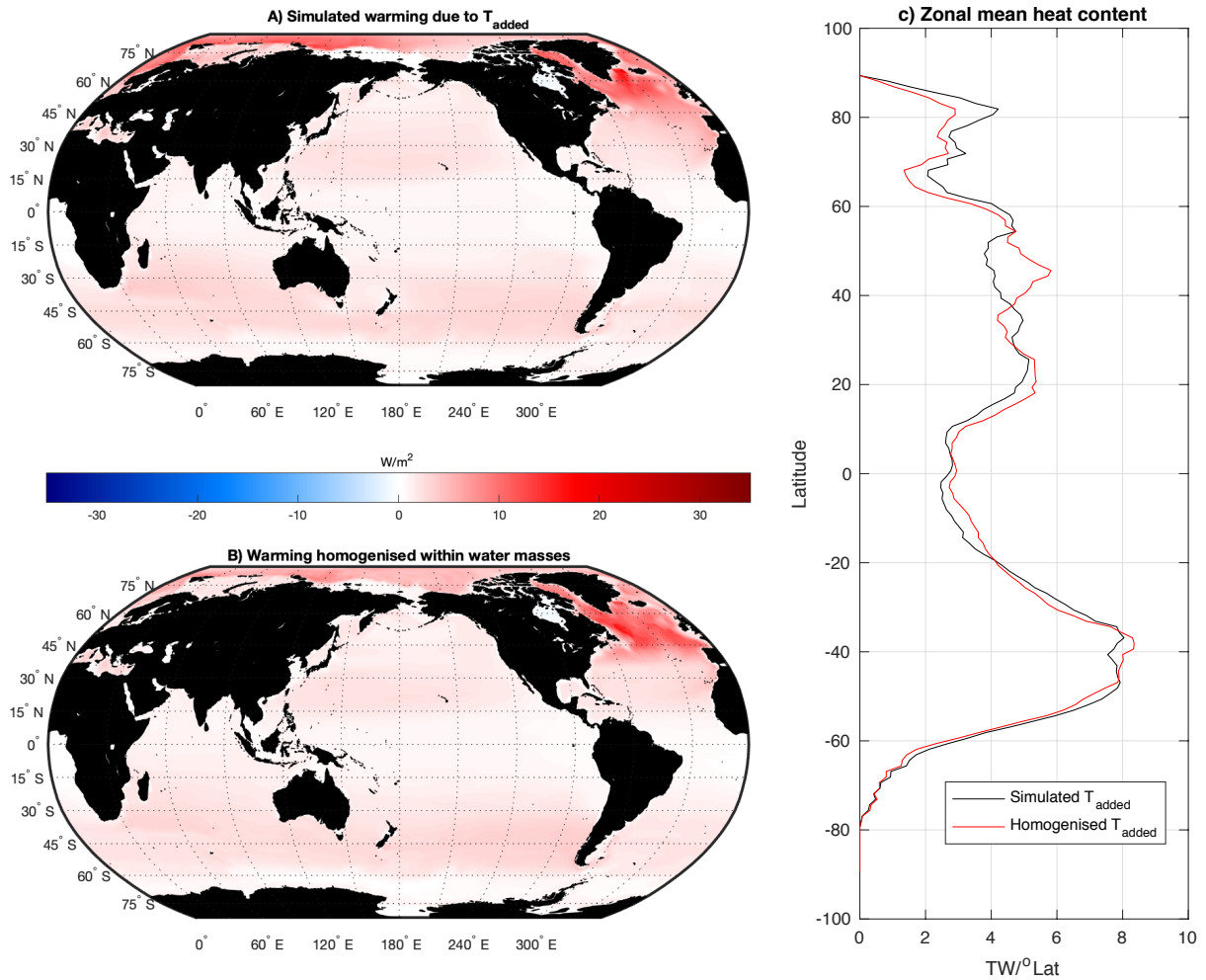
661 FIG. 3. Heterogeneous pattern of total and redistributed heat content change contrast against robust material
 662 heat content change. A: Change in depth integrated ocean heat content between years 2006-2011 and 2012-2017
 663 inclusive. B: Inferred redistributed heat and C: Inferred material heat content change based on changing water
 664 masses for the same period. Regions where the magnitude of the signal is less significant (less than two standard
 665 deviations of a bootstrap ensemble) are stippled.



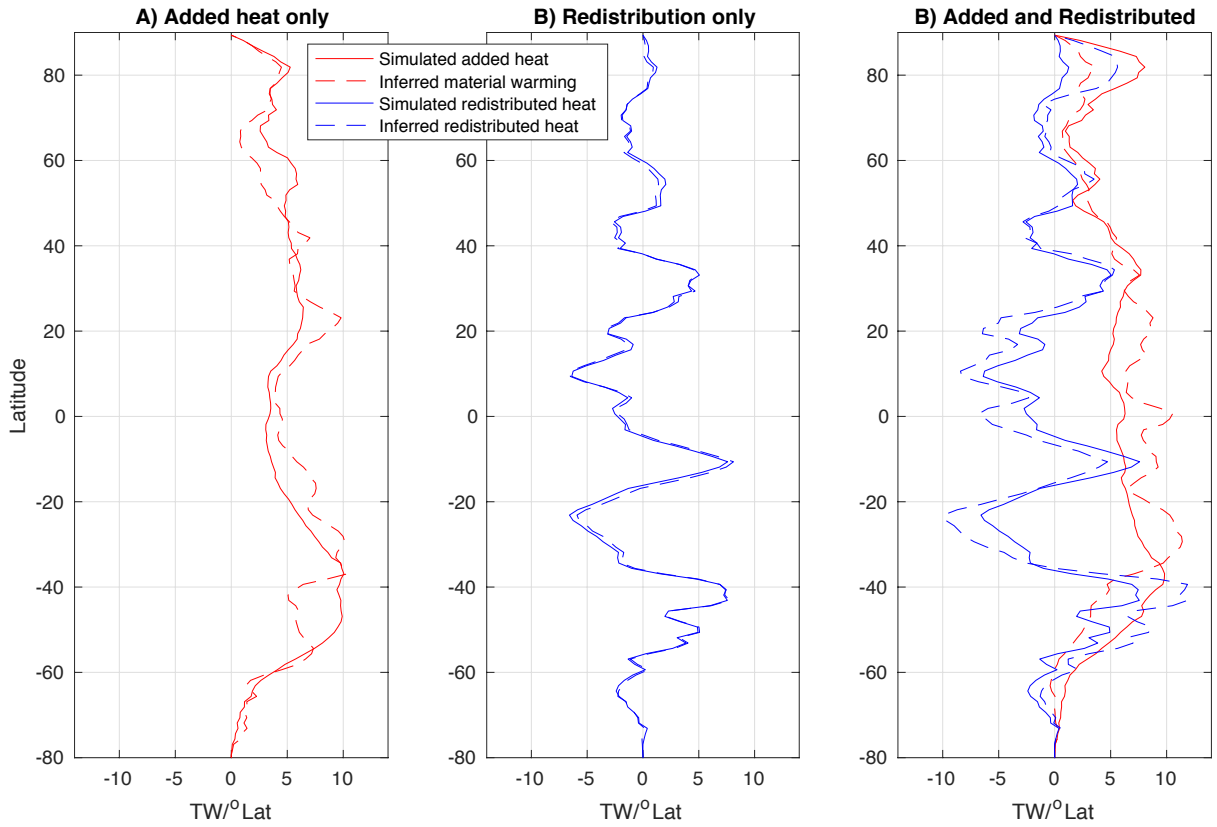
666 FIG. 4. Material heat content change is accumulating in the tropics and sub-tropics existing heat is being
 667 redistributed southward. A: Total heat content change (grey) redistribution contribution (blue) and material
 668 contribution (red). B: Contributions to material heat content change from the Indian (green), Pacific (orange)
 669 and Atlantic (yellow) Oceans. C: Meridional heat transport due to redistribution in the Southern Ocean (blue),
 670 Atlantic (cyan) and Indian plus Pacific Oceans (magenta). Estimates are bootstrap ensemble means with shading
 671 representing \pm two standard deviations.



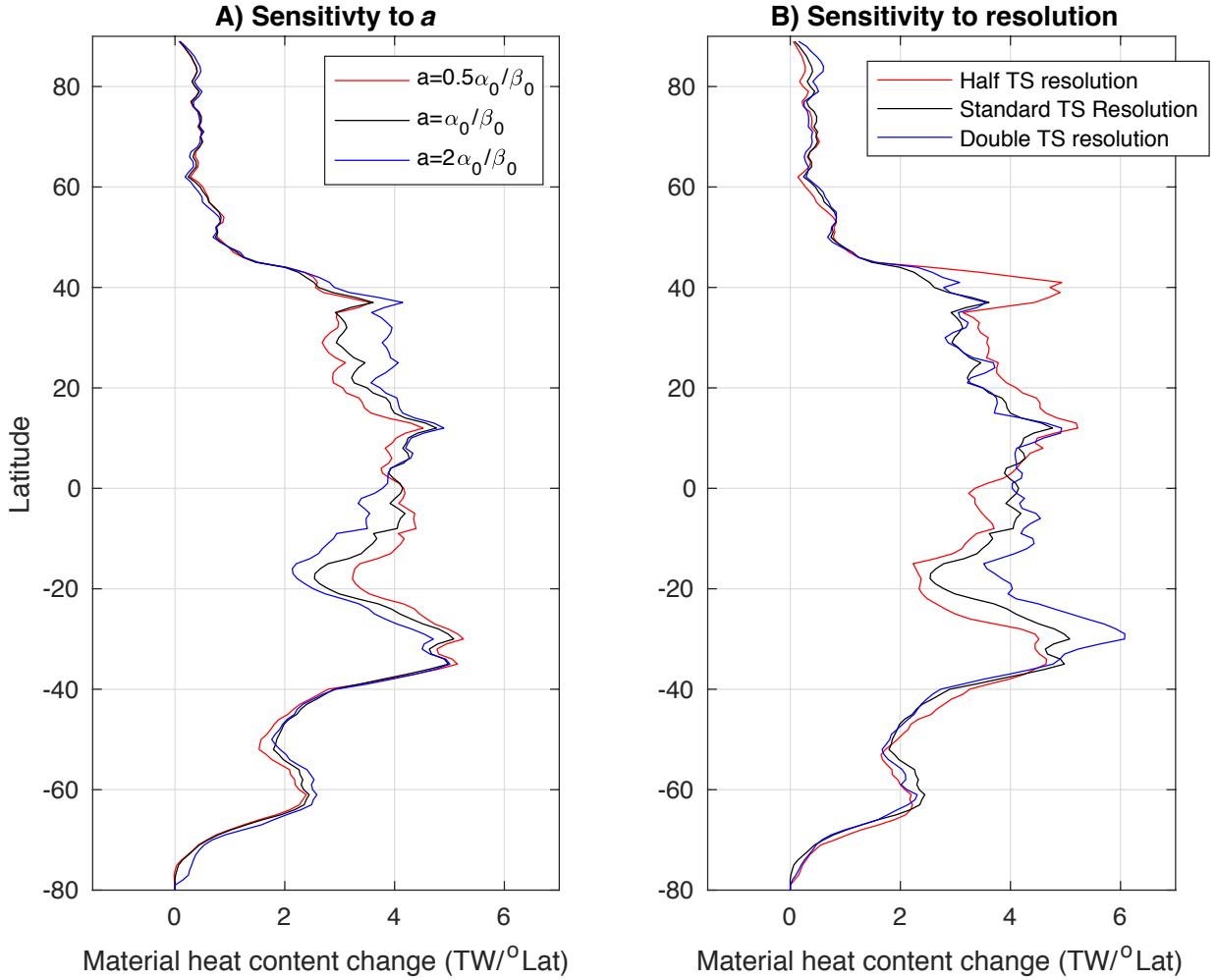
672 Fig. S1. Each marker shows $\Delta T_{material}$, the average warming required for each early water mass in order to
 673 transform them into the set of late water masses.



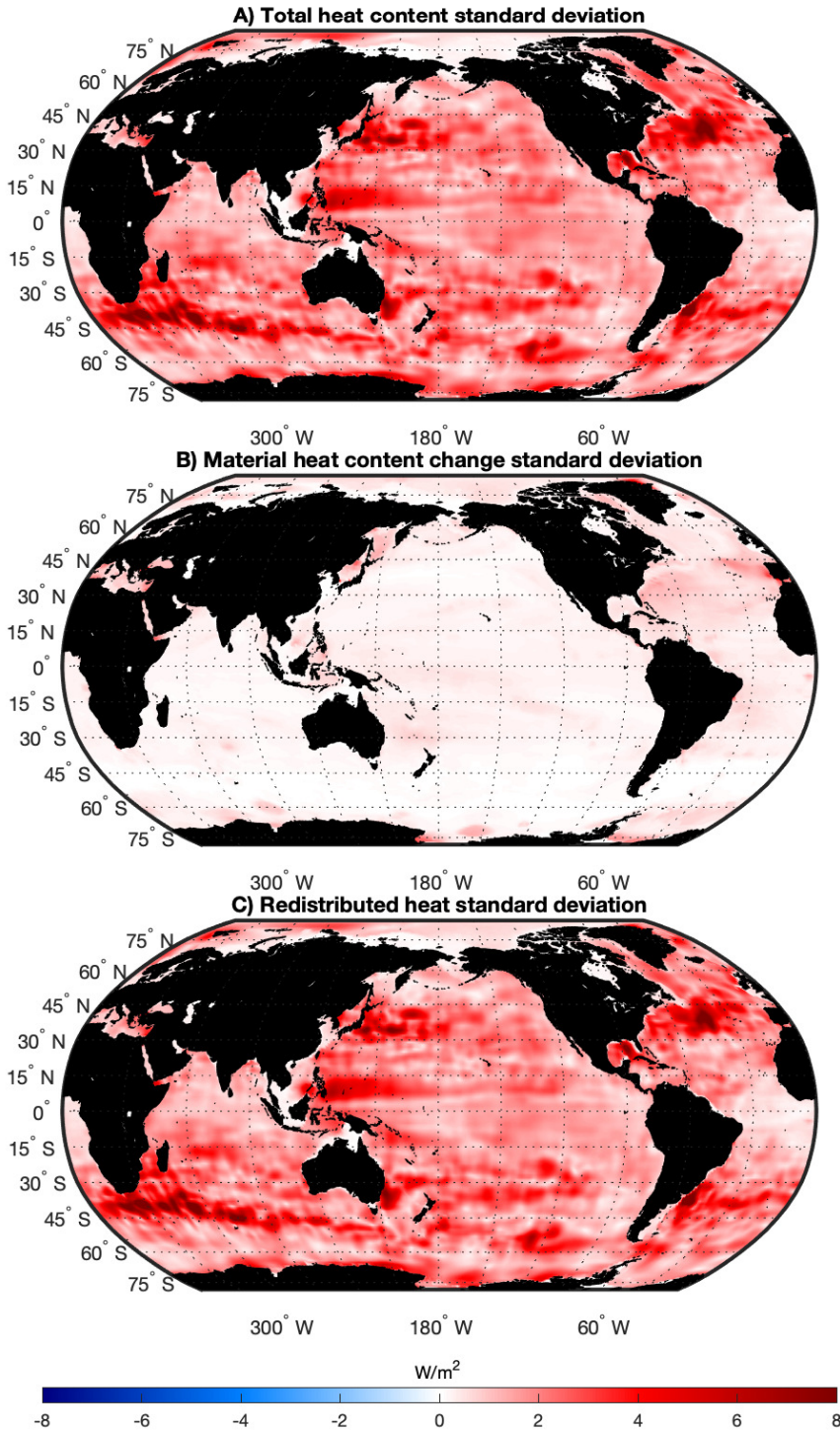
674 Fig. S2. A: Directly simulated added heat by the FAFheat experiment averaged over years 41-46 of the
 675 experiment. B: Inferred added heat when the same FAFheat data is first homogenized in water masses (bins in
 676 temperature-salinity coordinates) then remapped into the locations of those water masses over the same period.
 677 C: Comparison of the zonal integration of the two quantities shown in A and B.



678 Fig. S3. A: Zonally integrated simulated added heat (solid, red) and inferred material heat content change
 679 (dashed, red) based on our water mass method for years 41-46 of the *FAFheat* experiment comparing the
 680 simulation with and without added heat. B: Zonally integrated simulated heat content change (solid, blue) and
 681 inferred redistributed heat (dashed, blue) based on our water mass method comparing years 35-40 and 41-46 of
 682 the *piControl* experiment. C: Zonally integrated simulated added heat (solid, red) and redistributed heat (blue,
 683 solid) in the *FAFheat* experiment and inferred material heat content change (dashed, red) and redistributed heat
 684 (dashed, blue) based on our water mass method applied the model data.



685 Fig. S4. A: Zonally integrated inferred material heat content change for cases where the parameter a is set at
 686 a reference value of $a_0=\alpha_0/\beta_0 = 4.3\text{K}/(\text{g}/\text{kg})$ (black) and then reduced (red) and increased (blue) by a factor of
 687 two. B: Zonally integrated inferred material heat content change for cases where the $T - S$ bins are shrunk using
 688 a quadtree method until they either contain a volume of sea water less than $62 \times 10^{12}\text{m}^3$ or have a bin size of
 689 0.4°C by $0.2 \text{ g}/\text{kg}$ (black). Cases where the minimum volume is $15.5 \times 10^{12} \text{ m}^3$ and the minimum bin size is
 690 0.2°C by $0.1\text{g}/\text{kg}$ (blue) and where the minimum volume is $248 \times 10^{12} \text{ m}^3$ and the minimum bin size is 0.8°C
 691 by $0.4\text{g}/\text{kg}$ (red).



692 Fig. S5. A: One standard deviation of the heat content change inferred based on subsampling ‘early’ and ‘late’
 693 years of the EN4 data set. One standard deviation of the ensemble of inferred material heat content change (B)
 694 and redistributed heat (C) based on our water mass method applied to the same subsampled data as in A.